HHS Public Access

Author manuscript

IEEE Trans Radiat Plasma Med Sci. Author manuscript; available in PMC 2018 September 01.

Published in final edited form as:

IEEE Trans Radiat Plasma Med Sci. 2017 September ; 1(5): 405–415. doi:10.1109/TRPMS.2017.2725310

Molecular Breast Imaging using Synthetic Projections from High-Purity Germanium Detectors: A Simulation Study

Desmond Campbell [Member, IEEE] and **Todd Peterson [Member, IEEE]**

Department of Radiology and Radiological Sciences at Vanderbilt University Medical Center

Abstract

High-Purity Germanium (HPGe) gamma cameras are an emerging technology for Molecular Breast Imaging (MBI) due to their 2D lateral spatial resolution, depth-of-interaction (DOI) estimation, and superb energy resolution. In this simulation study, we investigate the potential imaging performance of an opposing view dual-head HPGe breast imaging system using a synthetic-projection technique, which utilizes DOI data with varying degrees of overlap in an iterative OSEM reconstruction algorithm to create 3D images from which new 2D projections are then created. The radiation transport simulator Monte Carlo N-Particle was employed to generate projections from 10-mm thick HPGe detectors using tungsten parallel-hole collimators with short and wide holes. Simulations modeling 140-keV emissions from various contrast-detail and breast-torso phantoms were conducted. Synthetic projections were generated along with conjugate-counting images from collected HPGe projections. Tumor contrast, SNR, and hot-spot detection measurements were used to compare images. Results show that the synthetic projections could resolve more low-contrast tumors compared to single-camera projections and conjugate-counting methods. MBI simulations also showed increased contrast and SNR in synthetic projections compared to individual projections. In conclusion, the HPGe imaging system employing a synthetic-projection technique may offer advantages over individual dual-camera projections or conjugate-counting methods in terms of contrast, SNR, and tumor detectability.

Index Terms

Molecular Breast Imaging; Germanium; Synthetic Projection; Monte Carlo

I. Introduction

Mammography has long been the gold standard for the screening and detection of breast cancer. However, mammography performance deteriorates when imaging dense breast tissue [1], [2]. Molecular Breast Imaging (MBI), also referred to as Breast Specific Gamma Imaging (BSGI), is a technique that utilizes specifically designed gamma cameras to image the distribution of a radiotracer, typically ^{99m}Tc-sestamibi, which exhibits higher uptake in malignant tissues than healthy tissue [3]. These techniques have less dependence on tissue density and higher sensitivity than mammography for the detection of sub-centimeter diameter tumors [4]–[13].

Originally, breast-specific cameras utilized scintillator crystals, such as Sodium Iodide, for gamma-ray detection with average energy resolution (ER) between 13%–17% FWHM at

140 keV and around 10% FWHM at 140 keV at best [14]–[16]. Some MBI systems now use semiconductor elements of Cadmium Zinc Telluride (CZT), which provide ~6.5% FWHM at 140 keV [6], [17]. In theory, the improved energy resolution should provide better scatter rejection and contrast for tumors when imaging in close proximity to the chest wall [18]. However, CZT detectors often suffer energy losses of absorbed gamma-rays due to incomplete charge collection, forming a tail of low-energy events beside the photopeak (tailing effect), and resulting in count-sensitivity losses if narrow energy windows are used. The semiconductor High-Purity Germanium (HPGe) offers the best energy resolution of any conventional radiation detector and does not suffer from the tailing effect [19]. Traditionally, these detectors required cooling with mounted liquid nitrogen dewars for optimal performance, making a compact imaging system for clinical and pre-clinical settings unrealistic. Recent technological advances have given rise to compact, mechanically-cooled HPGe gamma cameras that do not require bulky liquid nitrogen dewars. We have worked with an HPGe detector with a 8-cm diameter and of 10-mm thickness that offers ~1% ER at 140 keV and ~1.5 mm intrinsic spatial resolution in all three dimensions [20]. While this particular detector does not have a sufficiently large active area for MBI, herein, we investigate whether an HPGe detector of this type might offer some benefits for breast imaging.

We previously conducted simulations to examine the potential performance of a single breast-specific camera utilizing a conventional low-energy high-resolution, hexagonal-hole collimation using 10-mm-thick HPGe compared to a 5-mm thick CZT system. For equivalent activity imaged, the HPGe camera provided better relative sensitivity with similar tumor contrast and SNR while suppressing small-angle scatter events and background from the torso [21]. Other simulations investigating the feasibility of the HPGe camera with various parallel-hole collimators for MBI found that our choice of large-bore, square-hole collimation provided an 81% enhancement in count sensitivity and better suppression of events from the torso than the standard hexagonal-hole collimator [22].

A consequence of selecting large-bore collimation is the sacrifice of geometrical resolution for increased count sensitivity. However, it has been shown that utilizing depth-of-interaction (DOI) information in combination with an iterative reconstruction algorithm can compensate for collimator blurring to recover lost spatial resolution while maintaining an enhanced count sensitivity [7], [23], [24]. This concept is similar to the synthetic collimator [25], where projections collected with varying degrees of multiplexing (overlap projections from adjacent collimator openings) can be used to create images with better than expected spatial resolution. Initially, non-overlapped and multiplexed data were collected by changing pinhole-detector distances. However, we can use the DOI estimation capability of the HPGe detectors to acquire projections with different degrees of multiplexing at each detector depth. It has been determined that in 10-mm thick HPGe detectors, DOI effects can result in spatial resolution losses of 0.6 mm in pinhole SPECT [26]. Though the DOI effect may be less for our high-sensitive collimator, estimating depth events should provide a more accurate forward model and improve image resolution. Applying this processing scheme to our single HPGe camera model, we observed improved contrast in synthetic projections [27]. Although these reconstructed images lacked depth information due to the poor angular sampling of the

breast, attempts at limited-angle tomography have demonstrated some level of success, even with blurring artifacts from angular under-sampling [28]–[34].

A potential solution to further improve performance is utilizing a second HPGe camera opposite the first camera. Opposing dual-head gamma cameras were suggested as the preferred imaging geometry for compressed breast [14]. Using two NaI(Tl)-PSPMT cameras and multiplicative conjugate-counting methods for combining the projections has been shown to provide higher sensitivity for <10-mm tumors compared to a single-head imaging system in phantom studies [8], [35], [36]. A clinical CZT-based dual-head breast imaging system was found to have a 14% increase in sensitivity (from 41/61 to 50/61 cancers) for <10-mm tumors compared to a single camera based upon BI-RADS reader scores [37]. There are clear advantages to placing a second HPGe camera on the opposite side of the breast in our imaging geometry. An increase in tumor SNR may be expected due to approximately doubling the count sensitivity. Photons currently incident upon the lead compression pad in the single camera system could instead contribute to an additional projection image in a two-camera system. The second camera would also have a closer proximity to tumors that could be occult to the camera inferior to the breast due to attenuation and depth-dependent collimator blurring. These gains, observed in other dual-head cameras, may lead to increased detectability for small tumors using HPGe detectors [36], [37]. We also anticipate that utilizing synthetic projections with HPGe cameras will offer further advantages over just employing two cameras.

In this computational study, we investigate the potential imaging performance of an opposing-view dual-head HPGe breast imaging system using a synthetic-projection acquisition scheme and compare its performance against a single HPGe camera and traditional conjugate-counting methods.

II. Methods

In our previous study, a Monte Carlo model of an HPGe-based single-camera breast imaging system was developed using the Monte Carlo N-Particle (MCNP5) package [38]. The intrinsic properties of a benchtop HPGe detector were measured and used as inputs for our Monte Carlo model, followed by experimental validation of the model [21]. Current HPGe systems are not as large as those simulated here, however, this study serves as motivation to develop collimators and cameras of this type. In this study, we again utilized MCNP5 to generate projections for our dual-head breast imaging model. This single-camera model was extended to include a second camera superior to the breast. The event history, including the position of collisions, interaction type, propagating direction and energy, of particles that deposited energy into an HPGe detector was saved using MCNP5's PTRAC card. This information was analyzed within a MATLAB (MathWorks, Inc.) parser script to generate energy spectra and, subsequently, planar images from events falling within chosen energy windows.

A. HPGe Cameras

For these simulations, we modeled our HPGe detectors following the simulations of a CZT-based imaging system described in [39] and the architecture of our benchtop HPGe detector.

The two HPGe cameras were positioned opposing one another at a distance of 5.5 cm apart with one camera located inferior to the FOV and the other superior to it. We modeled the 10-mm thick HPGe detectors with 0.50-mm × 0.50-mm × 1-mm voxels within the 15-cm × 20-cm × 10-mm active volume, where the 1-mm thick voxels are based on the HPGe detector's DOI capability. 1.2×10^6 total detector voxels comprise each HPGe detector. A fixed ER of 1.0% FWHM at 140 keV and a lateral detector resolution of 1.5 mm FWHM were modeled based on measurements with our benchtop detector [20]. HPGe has an attenuation coefficient of 0.72 cm^{-1} at 140 keV, corresponding to an absorption efficiency of 51% in 10-mm thick HPGe cameras. An energy window of ±2.5% around the 140-keV photopeak was applied to discriminate against primary gamma-rays not depositing its full energy or scattered photons of lower energy. No depth blurring was applied to generated projections. Surrounding each detector was 4-mm thick lead shielding and an 1.5748-mm thick aluminum entrance window with a vacuum space of 11 mm.

Previous work into appropriate collimation for MBI suggests that registered collimators with bores matched to the detector elements maximizes the exposed active area of the detector and provides good collimation resolution in this unique, near-field imaging geometry [40]–[42]. The collimator employed in this study has been evaluated previously [22], but we briefly motivate its use here. Septal thickness was first chosen and positioned to shield the gap regions between collection strips in the benchtop HPGe detectors, with additional septa placed to improve geometric spatial resolution. The collimator length was selected to satisfy the Chicago criterion to ensure artifact-free projections and minimize septa penetration [43]. The mounted square-hole tungsten collimators had a 20-mm length, 2.25-mm hole width, and 0.25-mm septal thickness, providing an angular acceptance of 12.8°, an analytically calculated collimator resolution of 5.31 mm at 10-mm distance from the camera and a 83% increase in sensitivity (4.6×10^4 cpm/MBq) over a low-energy, high-resolution (LEHR) hexagonal-hole lead collimator with 20-mm length, 1.85-mm hole width, and 0.30-mm septal thickness (2.4×10^4 cpm/MBq)) [22].

Event positioning within the detectors was determined based on the first interaction within the crystal. For simplicity, no explicit modeling of the strip readout or the gap regions between strips was performed. Instead, energy blurring of 1.4 keV FWHM at 140 keV and spatial blurring of 1.5 mm FWHM was added to the model on an event-by-event basis using Gaussian distributions for the absorbed energy and the x- andl y-dimensions prior to binning.

B. Generation of Synthetic Projections

A transition from a conventional planar acquisition to a synthetic-projection acquisition scheme can be accomplished with the 3D position-estimation capability inherent to the HPGe detector in combination with wide-angle collimation. The differences between the traditional planar acquisition with an Anger camera and the approach with a detector that has DOI estimation are highlighted in figure 1. The short and wide bore of our parallel-hole collimator offers an increased angular view compared to conventional collimators. The shallow depths of the detectors provide high-count and low-multiplexed data, while the deep depths acquire projections with greater overlap. Incorporating these camera projections

within an iterative reconstruction generates a laterally-deblurred 3D image. Because the reconstructed image is expected to have poor depth resolution, the synthetic projections are produced by collapsing the depth information to form 2D planar images of two types. We generate the reprojection by summing the reconstructed image across depths and the Maximum Intensity Projection (MIP) by projecting the voxels with the largest values into the plane parallel to the cameras.

The forward problem can be represented mathematically as the following:

$$\mathbf{p}=\mathbf{H}\mathbf{f}+\mathbf{n}. \quad (1)$$

We apply the Ordered-Subset Estimation-Maximization (OSEM) iterative reconstruction algorithm to estimate **f**, the radioactivity distribution within the object, from collected projection data (**p**) with a priori knowledge of the system matrix (**H**) and zero noise (**n**) using the following equation:

$$f_j^{k+1}=\frac{f_j^k}{\sum_{i\in S}H_{ij}}\sum_{i\in S}H_{ji}\frac{p_i}{\sum_j H_{ij}f_j^k}, \quad (2)$$

where S refers to all detector pixels within the current subset [44]–[47]. A vectorized version of (2) can also be utilized with MATLAB if **H** is stored:

$$\mathbf{f^{k+1}}=\frac{\mathbf{f^k}}{\sum_{i\in S}H_{ij}}\mathbf{H^T}\frac{\mathbf{p}}{\mathbf{Hf^k}}, \quad (3)$$

where $\mathbf{H^T}$ represents the transpose of the system matrix. For the OSEM algorithm, each camera projection is treated as an individual subset, resulting in two subsets per iteration. Fifteen OSEM iterations were performed using the collected inferior and superior projections to generate and save 3D images from which the reprojection and MIP images were then created. Average normalized mean squared error (NMSE) was calculated for each iteration using (4) given the known radioactivity concentrations of the simulated phantoms:

$$Average\ NMSE=\frac{1}{n}\sum_j^n\left(\frac{f_j-g_j}{\bar{g}}\right)^2, \quad (4)$$

where f_j represents a reconstructed image voxel value, g_j represents a phantom voxel value, $\bar{g}$ is the mean activity of the phantom, and n is the number of discretized object voxels in the FOV, equal to 330,000.

The system matrix for the HPGe model was generated from Monte Carlo simulations. Utilizing Monte Carlo methods to generate **H** offers the benefit of inclusion of attenuation effects in the system matrix. Even though Monte Carlo simulations were employed to

acquire and save the system matrix, measuring the response by scanning a point source with a real imaging system would be one means to determine a system matrix that accounts for all geometrical and detector effects. MCNP5 simulations were conducted with a total of 1.9×10^{10} 140-keV gamma rays emitted in an 22.5° half-angle cone towards one HPGe detector. Even though 22.5° exceeds the angular acceptance of the collimator (12.8°), it allows for inclusion of small-angle scattered events in the system matrix. The 15-cm × 20-cm × 5.5-cm FOV was discretized into 1-mm × 1-mm × 5-mm voxels for a total of 330,000 object voxels. Asymmetrical object voxels were chosen due to the expected poor depth resolution. Symmetries in the image space allowed for simulating emissions uniformly from only 1/4 of the FOV, which reduced the computational burden. Approximately $5.9\overline{87}\times10^{6}$ gamma rays were emitted from each object voxel to generate its own point spread functions (PSF) within the HPGe detector. The PSFs originating from 1/4 of the FOV were flipped around the lines of symmetry to produce PSFs for the remainder of the inferior and superior camera's image space. The fraction of absorbed counts in the PSF to the total number of emissions from an object voxel determined the elements of the system matrix. The PSFs comprising the system matrix on average contain 5,508 counts across 1,098 detector elements. The generated $3.3\times10^{5}\times1.2\times10^{6}$ system matrix was incorporated into the OSEM reconstruction algorithm following (3) in order to perform synthetic-projection imaging using the two sets of projection data. The generated system matrix was only used for the OSEM reconstruction algorithm in this study and not as a projection operator for generating projection data for the phantom simulations.

C. Phantom Simulations

Here, we explain the geometric models and simulation parameters for the phantom studies. The simulations previously describing system matrix creation are separate and independent from the simulations used to generate the projection data from the phantoms.

First, a contrast-detail phantom was modeled to determine the image quality and detectability limits of various tumor sizes and activity concentrations. A diagram of the phantom is presented in figure 2. The phantom consisted of a 5×5 grid of tumors evenly spaced through the FOV. Tumor diameters varied from 2-mm to 10-mm in 2 mm increments and tumor-to-background ratios (TBR) ranged from 3:1 up to 20:1. All tissues were treated as water. Two different contrast-detail phantoms were simulated with tumors placed at either a 1-cm depth from the inferior camera or at the central depth, equidistant from both cameras. 2.0×10^{8} 140-keV photons were emitted in a cone beam with 22.5° half angle towards both the inferior and superior cameras, simulating a 10-minute scan with 4.9 MBq of activity within the phantom and generating clinically-relevant projections with ~1800 counts/cm^2 count density.

Second, we modeled a breast and torso water phantom based on the description of MBI simulations in [39]. A schematic diagram of the imaging simulation is shown in figure 3. The half-cylindrical breast had a thickness of 5.5 cm and a radius of 9.6 cm. Adjacent to the breast was a 20 cm × 20 cm × 20 cm box representing the torso, which contained a cylindrical heart and a cylindrical liver with heights of 9 cm and 14 cm, respectively, and radii of 3.50 cm and 5.25 cm, respectively. The breast contained three 1-cm diameter

spherical tumors located near the chest wall (tumor 1), in the center of the breast (tumor 2), and near the outer edge of the breast (tumor 3). Three different breast phantoms were simulated with the 1-cm diameter tumors placed either at a depth of 1 cm from the inferior camera, 2.25 cm (equidistant to both cameras) or 3.5 cm from the inferior camera (equivalent to 1 cm from the superior camera). Radioactivity concentrations and emission probabilities, the fraction of total emissions from an organ, were set from clinical studies for uptake of ^{99m}Tc-sestamibi following [39] and appear in table I. All tissues were treated as water. A total of 8.4×10^{10} 140-keV photons were emitted isotropically from the breast phantom, equivalent to injecting 740 MBq of ^{99m}Tc-sestamibi and imaging 157 MBq of activity within the breast phantom for 10 minutes, to generate clinically-relevant projections with ~1800 counts/cm^2 count density. Ten independent MBI simulations were conducted for tumors at each depth.

D. Image Processing

An objective of this investigation was to discern the potential benefits of the second set of projection data from the superior camera by leveraging the additional data using appropriate processing methods. For comparison purposes, we first considered the performance using the planar projections individually. Planar projections for the inferior and superior cameras were generated by summing the counts over each of the 10 detector depths. Conjugate-counting methods were employed to combine projections of opposing-view cameras, which suppress attenuation effects and generate a single planar image. The arithmetic (average) and geometric mean images were generated using the following:

$$\overline{I_A}=\frac{I_1+I_2}{2} \quad (5)$$

$$\overline{I_G}=\sqrt{I_1\times I_2}, \quad (6)$$

where I_1 and I_2 are the count values of opposing pixels in the inferior and superior cameras, respectively. Finally, OSEM reconstruction was performed using the inferior and superior projections with DOI information left intact, with reprojections and MIP images generated from the resultant 3D images.

E. Image Analysis

A single trial was conducted for each contrast-detail phantom with tumors at the two depths. A ±2.5% energy window around 140 keV was utilized for image generation. Camera projections for both the inferior and superior cameras, conjugate-counting projections, MIP and reprojected images were generated for the breast phantoms as described previously. Tumor contrast and SNR were calculated for each individual tumor by taking the mean and standard deviation of an adjacent 9×9 pixel ROI of background ($\bar{B}$, σ_B) and a 3×3 pixel ROI centered on the tumor ($\bar{T}$) and applying the following:

$$Contrast = \frac{\overline{T} - \overline{B}}{\overline{B}}, \quad (7)$$

$$SNR = \frac{\overline{T} - \overline{B}}{\sigma_B}. \quad (8)$$

In the case that the average NMSE curve failed to converge to a local minimum for reconstructed image selection, parametric contrast versus SNR curves were considered for determining the best reconstructed images [28].

A Hough transform algorithm for identifying circles above background was applied to the contrast-detail images to assess tumor detectability by determining the minimal SNR and size of hot spots [48]. The algorithm was tasked to identify 25 hot spots with diameters greater than 2 mm using the average background, $\bar{B}$, for each image as a minimum threshold. Identified circles were removed from each image to prevent double counting hot spots. Contrast-detail curves delineating the lowest contrast hot spot per tumor size identified by the Hough algorithm were drawn for each image type.

For the MBI simulations, simulated energy spectra parsed by the number of scatters and by event origin were produced for both cameras. To repeat, an energy window of ±2.5% around the 140-keV photopeak was applied to discriminate against primary photons which fail to deposit sufficient energy and to reject scattered photons. Camera projections for both the inferior and superior cameras, conjugate-counting projections, MIP, and reprojected images were generated for the breast phantoms as described previously. Relative count sensitivity, averaged over the three breast phantoms and normalized to the inferior camera, were calculated for the inferior and superior projections. We also calculated scatter and torso fractions, defined as the fraction of all events within the chosen energy window that scattered in the phantom and the fraction of all events within the chosen energy window that originated in the torso, respectively. Tumor contrast and SNR were calculated for each individual tumor using (7) and (8). ANOVA statistical analysis followed by student-t test with a 95% confidence interval was performed to compare contrast and SNR between the different image processing methods. In addition, an SNR threshold of 1.5, based on the results of the Hough transform algorithm to identify tumors, was employed to determine tumor visibility in breast projections.

III. Results

A. Contrast-Detail Simulations

Projections of the contrast-detail phantom with tumors at a 1-cm depth and central depth (equidistant from both HPGe cameras) were generated. For the synthetic-projection acquisition, the NMSE curves, displayed in figure 4a, show that tumors at the 1-cm and central depths have the most accurate images after four and two iterations, respectively. For

greater insight on appropriate stopping criterion for the OSEM reconstruction, parametric contrast versus SNR curves for select 1-cm diameter tumors are displayed in figure 4b. Although SNR monotonically decreased, the majority of SNR-constrast curves exhibited a maximum between 2 and 7 iterations. For the contrast-detail images, the iterations with the minimum NMSE are selected for further analysis. Select coronal slices through the tomographic images are shown in figure 5. The slices at these iterations illustrate the depth inaccuracy of the OSEM reconstruction with blurred activity along the acquisition axis.

Displayed in figures 6 and 7 are the collected and generated projections of the contrast-detail phantoms, with contrast-detail curves overlaid on each projection indicating the identified tumors from the Hough transform. The images of figure 6 indicate that the high quality data from the inferior camera, where the tumors are in close proximity, are able to compensate for the noisy data collected in the superior camera to generate reasonable combined-projections through conjugate-counting methods. However, this does not translate into tumor detectability for the conjugate-counting methods, as the Hough transform failed to identify the high-TBR, 4-mm hot spots that were detectable in the inferior image. The reprojection and the MIP exhibited higher image quality due to their low background intensities compared to the other projections, which enables identification of the high-TBR 4-mm hot spots as well as the large, low-TBR hot spots occult to the other methods. The same result is observed in figure 7, where the quality of the inferior and superior projections is low due to the larger source-to-detector distance for tumors located midway between. The single camera and combined projections are qualitatively equal, while the MIP and reprojection exhibit reduced background relative to the other methods. Because of this, the synthetic projections have more detectable tumors, including the 20:1 TBR, 4-mm diameter hot spot and the 5:1 TBR, 10-mm diameter hot spot. Correlating the Hough transform results with the measured SNR of the tumors, we determine that a SNR threshold of 1.5 is required for tumor detectability with this HPGe system. We apply this metric to the MBI results when describing tumor visibility.

B. MBI Simulations

Projection data from the two HPGe cameras were generated for the breast phantoms with tumors at varying depths. The pulse-height distributions for both HPGe cameras parsed by scatter order and event origin are shown in figure 8. The relative sensitivity and the scatter and torso fractions are tallied in table II. The addition of the superior camera grants an increase of 105% in count sensitivity, doubling the number of recorded events compared to the inferior camera alone. According to both scatter order spectra, greater than 90% of events in the 140-keV photopeak are primary counts, followed by first and second order scattered photons. The event origin spectra reveal that organs within the torso contribute to collected projections. The inferior camera still captures counts from the liver and heart due to gamma rays penetrating the lead shielding and due to small-angle scatters originating from the heart. However, the superior camera has a larger contribution of liver events due to lines of sight to the highly-radioactive liver, resulting in larger scatter and torso fractions for the superior camera.

The breast phantom projections for each camera for tumors at each of the three depths are shown in figure 9. The intensity of the hot spots in each image is inversely proportional to the distance between the HPGe camera and the tumors in the phantom. Using the SNR threshold of 1.5 for tumor visibility, the tumors at a 1 cm depth are visible in the inferior projection, while conversely, the tumors 3.5 cm from the superior camera are not visible from that view. The high-count region close to the chest wall heavily contaminates the superior projections and obscures the appearance of tumor 1. This artifact is due to the out-of-view contribution from the torso, specifically the highly radioactive liver. However, tumors 2 and 3 have SNR values greater than 1.5 when close to the superior camera and in the center of the FOV.

The projections generated for tumors at the various depths using conjugate-counting methods are displayed in figure 10. The average and geometric images for all depths are qualitatively similar, as the conjugate-counting technique is designed to suppress attenuation effects and generate depth-independent images. Tumors 2 and 3 are discernible, with SNR>1.5, but all images also exhibit the liver signal contamination from the superior projections that obscures tumor 1.

The NMSE curves for the 3D images with tumors at various depths are illustrated in figure 11a. For each breast phantom, the NMSE monotonically increases with increasing OSEM iteration. Rather than using the minimum of the NMSE curve as the reconstruction stopping criterion, the contrast and SNR of generated MIP and reprojection images are considered. Figure 11b displays representative parametric contrast-SNR curves for the MIP and reprojection of the breast image with tumors at a 2.25-cm depth. Given the 1.5 SNR-threshold deduced by the Hough transform, the improving contrast, and the small changes in NMSE in the early iterations, we selected the 3rd iteration, as it provides a fair tradeoff between contrast, SNR, and NMSE. The generated reprojection and MIP images from the third OSEM iteration are shown in figure 12. Tumor 2 and 3 are visible in all reconstructed images, independent of the tumor depth within the breast phantom. The signal contamination along the chest wall, originating in the superior projection, is present in all reconstructed projections and obscures tumor 1.

The average and standard deviations for contrast and SNR measurements for all methods of generated MBI projections are displayed in figure 13. Contrast measurements are higher for tumors in close proximity to the camera in single-camera projections, while tumors at the center depth are nearly equivalent for all methods. The two conjugate-counting methods have indistinguishable contrast and SNR measurements, which are nearly equivalent to the mean of the inferior and superior camera image quality metrics. The reprojection and MIP images tend to exhibit greater contrast and SNR than the other methods, including statistically higher contrast and SNR than the inferior camera alone except for tumors 2 and 3 at a 1-cm depth (figure 13a). Statistically significant differences in SNR are observed between the reprojection and MIP images and the inferior projection, with the reprojection exhibiting higher SNR than the MIP.

IV. Discussion

In this study, the imaging performance of an opposing dual-head HPGe breast imaging system using synthetic projection is compared to a single HPGe camera and two-camera conjugate-counting methods. Overall, the reprojection and MIP outperform the individual projections and combined planar images in terms of contrast, SNR, and tumor detection. In general, reprojecting the tomographic image offers the best contrast and SNR, although the MIP of the tomographic image provides nearly equivalent contrast in breast phantom scans and detection capability for the contrast-detail phantom.

A limitation of this simulation work is the usage of a simplistic breast and torso phantom with a set body habitus and breast thickness. Likewise, adopting an anthropomorphic model, such as the XCAT phantom, would provide a more realistic ^{99m}Tc-sestamibi source distribution. However, more important than simulating a realistic phantom is selecting an appropriate geometry for radiation transport. Selection of the simulation geometry was based on obtained measurements of compressed breast thicknesses and widths from a large sample population, which produced accurate energy spectra from MBI scans using a CZT-based camera [39]. Relevant information on the expected performance of these cameras can be observed with these models. Only the average body habitus is modeled in this work and variations in patient habitus could change measured image quality and performance of the dual-head HPGe system.

Scattered events contribute to the intensity and variance of the background, which lowers contrast and SNR. In our previous work comparing a single HPGe and CZT camera for breast imaging, we observed higher scatter fractions for CZT than HPGe (8.63% CZT versus 4.66% HPGe) [21]. This was due to the large asymmetric 15% energy window needed for CZT due to poorer energy resolution (~6.5% FWHM at 140 keV) and its low-energy tailing effect [6], [17]. The advantage of HPGe detectors is their 1% FWHM energy resolution, which enables tight energy discrimination. The absence of tailing effects observed in CZT serves as an additional advantage for HPGe detectors. Finally, the moderate stopping power of HPGe allows for counts to be absorbed in deeper depths, a necessity for this synthetic projection imaging. From our previous simulations, CZT and HPGe exhibited equivalent performance in terms of contrast and SNR, while reducing the injected radioactivity by 25% for the HPGe simulations. This reduction in injected radiotracer should translate to lower radiation dose and exposure to MBI subjects. A conventional lead collimator was used in the previous simulation study instead of the tungsten collimator employed in this manuscript, however, we observed similar scatter and torso fractions between the inferior HPGe cameras utilized here and previous work. Thus, we deduce that the scatter fractions in these HPGe images are small enough to not impact contrast, SNR, and lesion detection.

Throughout this work with synthetic-projection imaging, the NMSE curves from reconstructed images tend to monotonically increase following a small number of iterations. The insufficient angular sampling leads to poor depth resolution and large NMSE values, as seen in figure 4 and 5. We hypothesize that the NMSE curve minimums occur in the first few iterations because the phantoms being reconstructed consist of a uniform background, a small number of hot spheres, and no randomized structure. In addition, the OSEM

reconstruction algorithm is initialized assuming an uniform source activity distribution. Because the initial guesses and phantoms are fairly similar, the first few iterations yield the lowest error. Background parenchymal uptake of sestamibi yields non-uniform structure in breast projections [49], which may require additional OSEM iterations to resolve. A consequence of more OSEM iterations would be further reductions in SNR, but with a potential increase in contrast as observe in generated parametric curves 4 and 11. To investigate this behavior further, more sophisticated phantoms with greater anatomic structure will have to be modeled.

Upon close observation of the coronal slices from the tomographic contrast-detail images in figure 5, although the activity is blurred across several voxels, the activity profiles differ for tumors located at different depths. The activity for the 1-cm depth tumors is concentrated near the inferior camera, while the centralized tumors exhibit a more uniform spread across the FOV. This could indicate some small amount of depth localization for tumors. However, additional simulations are required to determine the degree of depth sensitivity.

For the breast phantom simulations, the performance of the superior camera is impeded by the high liver activity. This is reflected in table II, which lists the high 8.5% torso fraction of events for the superior camera compared to the inferior camera at 2.98%. Quantitatively, the image quality of the superior camera projections are comparable to the inferior camera. However, the liver signal contamination encompasses tumor 1 and obstructs its visualization as seen in figure 9a. Furthermore, the liver signal contamination is carried over to the combined conjugate-counting and the synthetic-projection images in figure 10 and figure 12, hindering tumor detection along the chest wall. This ultimately raises questions on the accuracy of the contrast and SNR measurements for tumor 1. However, the lack of image artifacts around tumors 2 and 3 enables us to draw conclusions on breast imaging performance using the synthetic-projection scheme. For this imaging system to exhibit more reliable imaging performance along the chest wall, MBI technologists could position the cameras away from the torso in order to reduce the out-of-view contributions from the liver. Adjustments to the dual-head imaging system, such as employing slightly different parallel-hole collimation, may be required to avoid viewing the torso and enable improved tumor detection near the chest wall. With proper positioning or collimation, the advantages and benefits of using this HPGe camera could be extended towards the chest wall region.

The asymmetric image quality between inferior and superior projections is concerning for the efficacy of average and geometric projections. Combining low-quality and high-quality datasets using conjugate-counting methods yields projections with worse image quality than the higher-quality projection alone. With similar planar images (where tumors are equidistant from each camera), little improvement in image quality or detectability is observed in average or geometric mean projections. Thus, conjugate-counting methods appear to offer no benefit beyond conventional planar imaging with HPGe cameras. Reviewing the individual projections simultaneously, or only viewing the image from the detector closest to the tumor, would appear to be sufficient when synthetic projections from tomographic reconstruction are not available.

V. Conclusion

Monte Carlo simulations using an opposing-view, dual-head HPGe imaging system were conducted to investigate potential image processing methods and their impact on tumor detection in MBI. Adding a second camera superior to the breast provided increased count sensitivity when a synthetic-projection scheme was employed. Findings reveal that incorporating both sets of projection data into an OSEM reconstruction algorithm grants equivalent to better image performance for MBI and tumor detection capability for low-contrast tumors over single-camera planar imaging and two-camera conjugate-counting approaches. If the effect of the liver background can be reduced, the increased count sensitivity, image quality, and tumor detectability afforded by synthetic projection using a dual-head HPGe system would make it a worthwhile pursuit.

Acknowledgments

This work was conducted in part using the resources of the Advanced Computing Center for Research and Education at Vanderbilt University, Nashville, TN. We would like to thank the Ionizing Imaging group at the Vanderbilt University Institute of Imaging Science, Dr. Sepideh Shokouhi, Dr. M. Noor Tantawy, and Rose Perea. Additional thanks to PHDs Co. and Dilon Technologies for their support and assistance through this work. This work was supported by NIH/NIBIB R44EB15889, NIH/NIBIB R01EB013677, NIH/NCI R25CA136440, and the Southern Regional Education Board.

References

1. Rosenberg RD, Hunt WC, Williamson MR, Gilliland FD, Wiest PW, Kelsey CA, Key CR, Linver MN. Effects of age, breast density, ethnicity, and estrogen replacement therapy on screening mammographic sensitivity and cancer stage at diagnosis: review of 183,134 screening mammograms in Albuquerque, New Mexico. Radiology. 1998; 209:511–518. [PubMed: 9807581]
2. Pisano ED, Hendrick RE, Yaffe MJ, Baum JK, Acharyya S, Cormack JB, Hanna LA, Conant EF, Fajardo LL, Bassett LW, et al. Diagnostic accuracy of digital versus film mammography: exploratory analysis of selected population subgroups in dmist 1. Radiology. 2008; 246(2):376–383. [PubMed: 18227537]
3. Delmon-Moingeon LI, Piwnica-Worms D, Van den Abbeele AD, Holman BL, Davison A, Jones AG. Uptake of the cation hexakis (2-methoxyisobutylisonitrile)-technetium-99m by human carcinoma cell lines in vitro. Cancer Res. 1990; 50(7):2198–2202. [PubMed: 2317808]
4. Garibaldi F, Cisbani E, Colilli S, Cusanno F, Fratoni R, Giuliani F, Gricia M, Lucentini M, Lo Meo S, Magliozzi ML, Santanvenere F, Cinti MN, Pani R, Pellegrini R, Simonetti G, Schillaci O, Del Vecchio S, Salvatore M, Majewski S, Lanza RC, De Vincentis G, Scopinaro F. Molecular imaging: High-resolution detectors for early diagnosis and therapy monitoring of breast cancer. Nucl Instr & Meth Phys Rese A. 2006; 569:286–290.
5. Tornai, MP., Brzymialkiewicz, CN., Cutler, SJ., Madhav, P. Comparison of scintimammography and dedicated emission mammotomography. Nuclear Science Symposium Conference Record, 2004 IEEE; IEEE; 2004. p. 2818-2822.
6. Mueller B, OConnor MK, Blevis I, Rhodes DJ, Smith R, Collins DA, Phillips SW. Evaluation of a small cadmium zinc telluride detector for scintimammography. J Nucl Med. 2003; 44:602–609. [PubMed: 12679406]
7. Robert C, Montémont G, Rebuffel V, Verger L, Buvat I. Optimization of a parallel hole collimator/CdZnTe gamma-camera architecture for scintimammography. Med Phys. 2011; 38:1806. [PubMed: 21626915]
8. Judy PG, Gong Z, Dinion NL, Welch BL, Saviour TS, Kieper D, Majewski S, McKisson J, Kross B, Proffitt J, Stolin AV, More MJ, Villiams MB. Analysis of image combination methods for conjugate breast scintigraphy. IEEE Trans Nucl Sci. 2010; 57:1146–1154.

9. Rhodes DJ, Hruska CB, Phillips SW, Whaley DH, Oconnor MK. Dedicated dual-head gamma imaging for breast cancer screening in women with mammographically dense breasts 1. Radiology. 2011; 258(1):106–118. [PubMed: 21045179]
10. Rhodes DJ, Hruska CB, Conners AL, Tortorelli CL, Maxwell RW, Jones KN, Toledano AY, O'Connor MK. Journal club: Molecular breast imaging at reduced radiation dose for supplemental screening in mammographically dense breasts. American Journal of Roentgenology. 2015; 204(2): 241–251. [PubMed: 25615744]
11. Brem RF, Ruda RC, Yang JL, Coffey CM, Rapelyea JA. Breast-specific γ-imaging for the detection of mammographically occult breast cancer in women at increased risk. Journal of Nuclear Medicine. 2016; 57(5):678–684. [PubMed: 26823569]
12. Rechtman LR, Lenihan MJ, Lieberman JH, Teal CB, Torrente J, Rapelyea JA, Brem RF. Breast-specific gamma imaging for the detection of breast cancer in dense versus nondense breasts. American Journal of Roentgenology. 2014; 202(2):293–298. [PubMed: 24450668]
13. Shermis RB, Wilson KD, Doyle MT, Martin TS, Merryman D, Kudrolli H, Brenner RJ. Supplemental breast cancer screening with molecular breast imaging for women with dense breast tissue. American Journal of Roentgenology. 2016:1–8.
14. Majewski S, Kieper D, Curran E, Keppel C, Kross B, Palumbo A, Popov V, Wisenberger A, Welch B, Wojcik R, Williams MB, Goode AR, More M, Zhang G. Optimization of dedicated scintimammography procedure using detector prototypes and compressible phantoms. Nuclear Science, IEEE Transactions on. 2001; 48(3):822–829.
15. Kieper D, Majewski S, Kross B, Popov V, Weisenberger A, Welch B, Wojcik R, Williams M, Goode A, More M, et al. Optimization of breast imaging procedure with dedicated compact gamma cameras. Nuclear Instruments and Methods in Physics Research Section A: Accelerators, Spectrometers, Detectors and Associated Equipment. 2003; 497(1):168–173.
16. Moré, MJ., Goodale, PJ., Majewski, S., Williams, MB. Evaluation of gamma cameras for use in dedicated breast imaging. Nuclear Science Symposium Conference Record, 2004 IEEE; IEEE; 2004. p. 3658-3662.
17. Rhodes, DJ., O'Connor, MK., Phillips, SW., Smith, RL., Collins, DA. Mayo Clinic Proceedings. Vol. 80. Elsevier; 2005. Molecular breast imaging: a new technique using technetium tc 99m scintimammography to detect small tumors of the breast; p. 24-30.
18. Hruska CB, O'Connor MK. Czt detectors: How important is energy resolution for nuclear breast imaging? Physica Medica. 2006; 21:72–75. [PubMed: 17645999]
19. Johnson LC, Campbell DL, Hull EL, Peterson TE. Characterization of a high-purity germanium detector for small-animal spect. Phys Med Biol. 2011; 56(18):5877. [PubMed: 21852723]
20. Johnson, LC., Campbell, DL., Ovchinnikov, OS., Peterson, T. Performance characterization of a high-purity germanium detector for small-animal spect. Nuclear Science Symposium and Medical Imaging Conference (NSS/MIC), 2011 IEEE; IEEE; 2011. p. 607-612.
21. Campbell D, Peterson T. Simulation study comparing high-purity germanium and cadmium zinc telluride detectors for breast imaging. Physics in Medicine and Biology. 2014; 59(22):7059. [PubMed: 25360792]
22. Campbell, DL., Peterson, TE. Evaluating collimator designs for nuclear breast imaging with high-purity germanium detectors. Nuclear Science Symposium and Medical Imaging Conference (NSS/MIC), 2011 IEEE; IEEE; 2011. p. 2743-2748.
23. Guerin L, Verger L, Rebuffel V, Monnet O. A new architecture for pixellated solid state gamma camera used in nuclear medicine. Nuclear Science, IEEE Transactions on. 2008; 55(3):1573–1580.
24. Robert C, Montémont G, Rebuffel V, Buvat I, Guérin L, Verger L. Simulation-based evaluation and optimization of a new cdznte gamma-camera architecture (hisens). Physics in medicine and biology. 2010; 55(9):2709. [PubMed: 20400808]
25. Wilson D, Barrett HH, Clarkson EW. Reconstruction of two-and three-dimensional images from synthetic-collimator data. IEEE transactions on medical imaging. 2000; 19(5):412–422. [PubMed: 11021685]
26. Hwang, AB., Iwata, K., Hasegawa, BH. Simulation of depth of interaction effects for pinhole spect. Nuclear Science Symposium Conference Record, 2001 IEEE; IEEE; 2001. p. 1293-1297.

27. Campbell, D., Peterson, T. Simulations investigating the impact of depth-of-interaction in nuclear breast imaging with a dedicated germanium gamma camera. Nuclear Science Symposium and Medical Imaging Conference (NSS/MIC), 2012 IEEE; IEEE; 2012. p. 2718-2722.
28. Tornai MP, Bowsher JE, Archer CN, Peter J, Jaszczak RJ, MacDonald LR, Patt BE, Iwanczyk JS. A 3d gantry single photon emission tomograph with hemispherical coverage for dedicated breast imaging. Nuclear Instruments and Methods in Physics Research Section A: Accelerators, Spectrometers, Detectors and Associated Equipment. 2003; 497(1):157–167.
29. Smith MF, Majewski S, Weisenberger AG, Kieper DA, Raylman RR, Turkington TG. Analysis of factors affecting positron emission mammography (pem) image formation. IEEE Transactions on Nuclear Science. 2003; 50(1):53–59.
30. Williams MB, Judy PG, Gunn S, Majewski S. Dual-modality breast tomosynthesis 1. Radiology. 2010; 255(1):191–198. [PubMed: 20308457]
31. Perez KL, Cutler SJ, Madhav P, Tornai MP. Towards quantification of functional breast images using dedicated spect with non-traditional acquisition trajectories. Nuclear Science, IEEE Transactions on. 2011; 58(5):2219–2225.
32. Gong Z, Klanian K, Patel T, Sullivan O, Williams MB. Implementation and evaluation of an expectation maximization reconstruction algorithm for gamma emission breast tomosynthesis. Medical physics. 2012; 39(12):7580–7592. [PubMed: 23231306]
33. Gopan O, Gilland D, Weisenberger A, Kross B, Welch B. Molecular imaging of the breast using a variable-angle slant-hole collimator. IEEE Transactions on Nuclear Science. 2014; 61(3):1143–1152.
34. Gong Z, Williams MB. Comparison of breast specific gamma imaging and molecular breast tomosynthesis in breast cancer detection: Evaluation in phantoms. Medical physics. 2015; 42(7): 4250–4259. [PubMed: 26133623]
35. Majewski S, Black R, Kross B, Popov V, Welch B, Wojécik R, Williams M, Moré M, Goodale P. Phantom evaluations of a dedicated dual-head scintimammography system. Physica Medica. 2006; 21:35–38. [PubMed: 17645991]
36. Judy, PG., Welch, B., St Saviour, T., Kieper, D., Majewski, S., McKisson, J., Kross, B., Proffitt, J., Stolin, A., More, MJ., Dinion, NL., Williams, MB. Molecular breast imaging with directly opposing compact gamma cameras. Nuclear Science Symposium Conference Record, 2007. NSS'07. IEEE; IEEE; 2007. p. 4040-4043.
37. Hruska CB, Phillips SW, Whaley DH, Rhodes DJ, OConnor MK. Molecular breast imaging: use of a dual-head dedicated gamma camera to detect small breast tumors. AJR. American journal of roentgenology. 2008; 191(6)
38. Brown FB, Barrett R, Booth T, Bull J, Cox L, Forster R, Goorley T, Mosteller R, Post S, Prael R, et al. MCNP version 5. Trans Am Nucl Soc. 2002; 87:4 4.
39. Hruska CB, O'Connor MK. A monte carlo model for energy spectra analysis in dedicated nuclear breast imaging. Nuclear Science, IEEE Transactions on. 2008; 55(1):491–500.
40. Gruber G, Moses W, Derenzo S. Monte carlo simulation of breast tumor imaging properties with compact, discrete gamma cameras. IEEE Transactions on Nuclear Science. 1999; 46(6):2119–2123.
41. Hruska CB, O'Connor MK. Effect of collimator selection on tumor detection for dedicated nuclear breast imaging systems. IEEE transactions on nuclear science. 2006; 53(5):2680–2689.
42. Weinmann AL, Hruska CB, O'Connor MK. Design of optimal collimation for dedicated molecular breast imaging systems. Medical physics. 2009; 36(3):845–856. [PubMed: 19378745]
43. Gunter, DL. Emission tomography: the fundamentals of PET and SPECT. San Diego, London: Elsevier Academic; 2004. Collimator design for nuclear medicine; p. 153-68.
44. Rockmore AJ, Macovski A. A maximum likelihood approach to emission image reconstruction from projections. Nuclear Science, IEEE Transactions on. 1976; 23(4):1428–1432.
45. Shepp LA, Vardi Y. Maximum likelihood reconstruction for emission tomography. Medical Imaging, IEEE Transactions on. 1982; 1(2):113–122.
46. Lange K, Carson R. Em reconstruction algorithms for emission and transmission tomography. J Comput Assist Tomogr. 1984; 8(2):306–316. [PubMed: 6608535]

47. Hudson HM, Larkin RS. Accelerated image reconstruction using ordered subsets of projection data. Medical Imaging, IEEE Transactions on. 1994; 13(4):601–609.

48. Duda RO, Hart PE. Use of the hough transformation to detect lines and curves in pictures. Communications of the ACM. 1972; 15(1):11–15.

49. Hruska CB, Scott CG, Conners AL, Whaley DH, Rhodes DJ, Carter RE, OConnor MK, Hunt KN, Brandt KR, Vachon CM. Background parenchymal uptake on molecular breast imaging as a breast cancer risk factor: a case-control study. Breast Cancer Research. 2016; 18(1):42. [PubMed: 27113363]

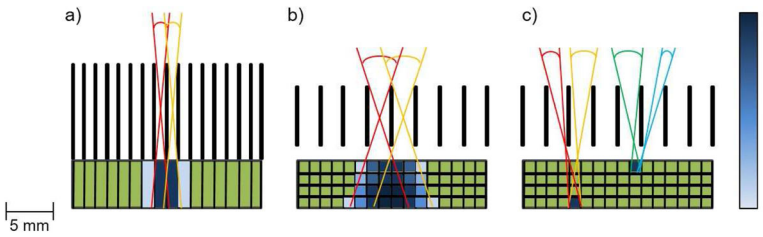

Fig. 1.

Schematic diagrams showing the differences between the traditional planar acquisition and the synthetic-projection approach. a) The conventional parallel-hole collimator mounted to a detector without DOI estimation. b) and c) A collimator with wider and shorter bores mounted to a detector with 3D position sensitivity. The color pixels within the detector represents the amount of overlap in the angular view (multiplexing) of adjacent collimator bores. The highly-sensitive collimator provides greater angular acceptance than the conventional collimator, but at the cost of spatial resolution. However, combining multiplexed data at different depths within an iterative reconstruction algorithm can generate images with recovered resolution.

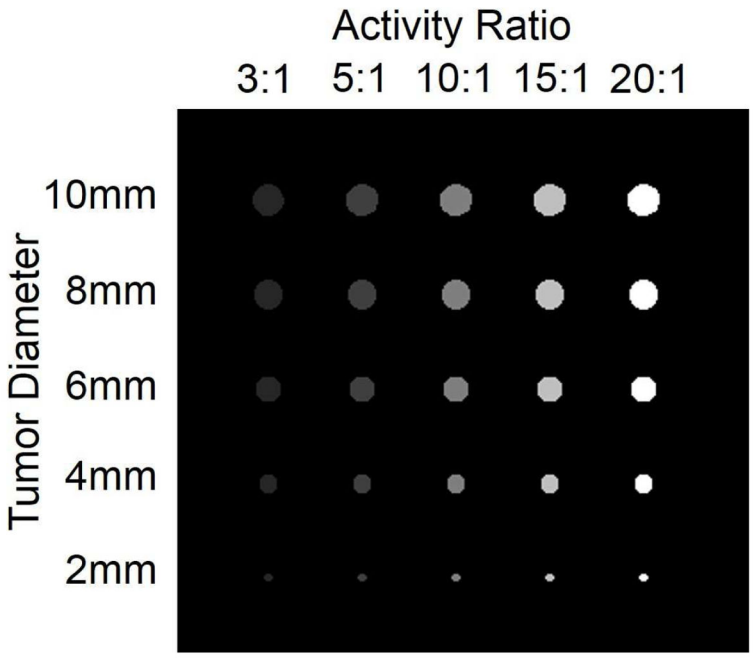

Fig. 2.

An axial view of the contrast-detail phantom developed for investigating tumor detectability. Tumor diameters are labeled along the right and TBRs are labeled on top. Lighter color circles denote higher radioactivity concentrations, labeled on top. Tumor diameter, depth, and activity concentrations are varied for determining limits of SNR measurements and hot spot identification.

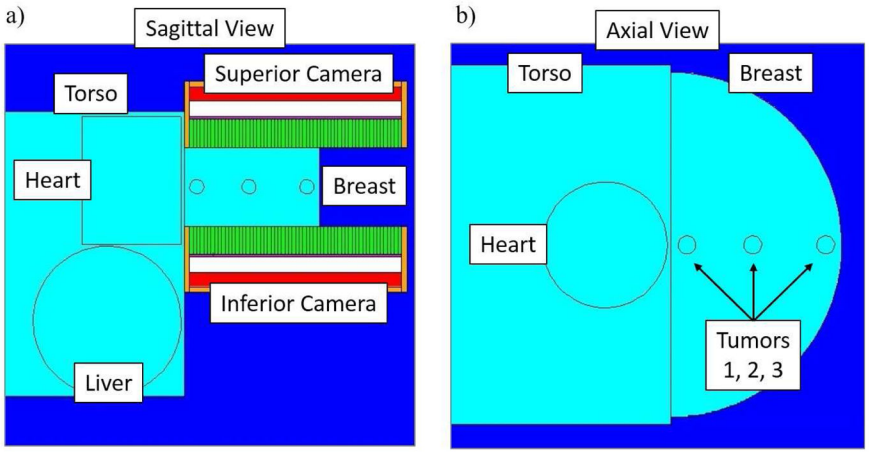

Fig. 3.

The geometry for the Monte Carlo MBI simulations with the dual-head HPGe imaging system. a) The sagittal view of the model and b) the axial view of the breast phantom. The MBI simulation geometry includes the inferior and superior HPGe cameras encased in 4-mm thick lead shielding. The half-cylindrical breast contains three 1-cm diameter spherical tumors located near the chest wall (tumor 1), in the center of the breast (tumor 2), and near the anterior edge of the breast (tumor 3). Tumors are placed at either 1-cm, 2.25-cm, or 3.5-cm depths. The torso contains a cylindrical heart and liver.

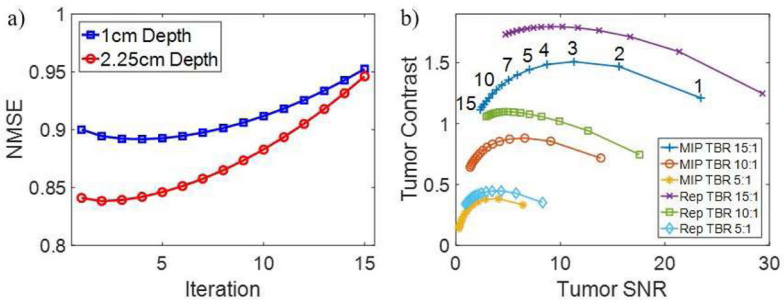

Fig. 4.

a) The NMSE curves of the OSEM reconstructed contrast-detail images containing tumors at the 1-cm and 2.25-cm depth. The curves indicate that the fourth and second iterations for tumors at the 1-cm and 2.25-cm depths have the most accurate images, respectively. b) A contrast versus SNR parametric curves for select 1-cm diameter tumors at the 2.25-cm depth in the MIP and reprojection (Rep) images. The black numbers indicate iteration number. The curves tend to reach a maximum tumor contrast between the second and seventh iteration, but at the cost of SNR.

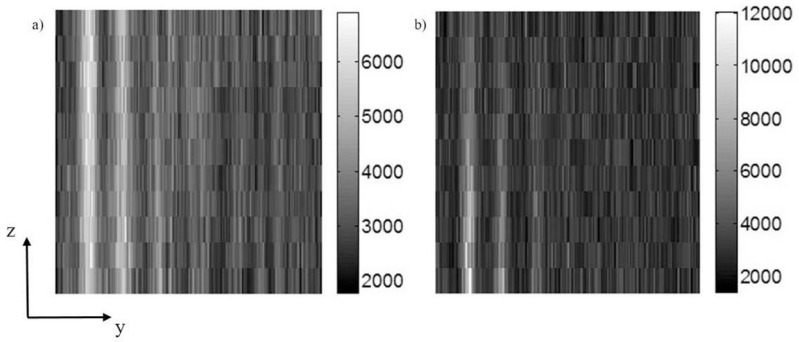

Fig. 5.

Coronal slices of the 3D images with the lowest NMSE through the 10:1 TBR tumors located at a) the 2.25-cm depth and b) the 1-cm depth. The origin of the coordinate system lays in the same plane as the inferior HPGe camera, with the z-axis oriented normal to the camera. The two slices exhibit different activity profiles along the axis normal to both HPGe cameras, making tumor depth localization difficult to estimate, but indicative of some depth sensitivity.

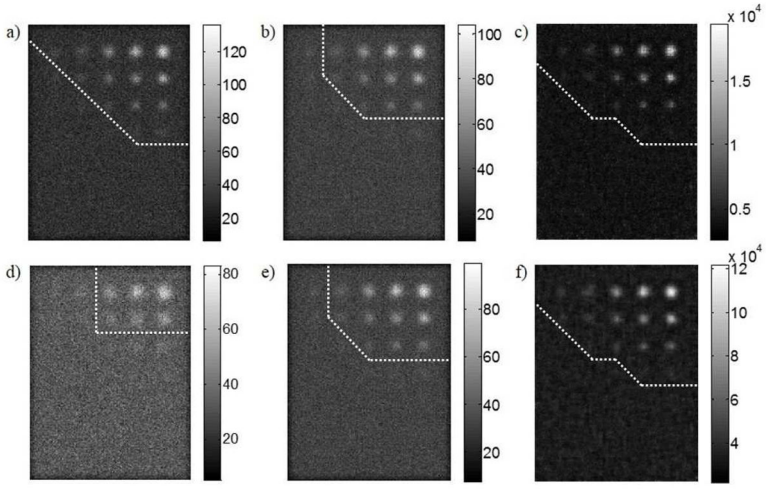

Fig. 6.

Contrast-detail projections of tumors at a 1-cm depth. Top row: a) Inferior, b) Average, c) MIP. Bottom row: d) Superior, e) Geometric mean, f) Reprojection. Colorbar units are in counts for the planar projections and in number of emissions for the reconstructed projections. Tumors identified by the Hough transform algorithm are located above and to the right of the dashed contrast-detail curve overlaid on each projection. The synthetic projections contained the most identified hot spots, including the 8-mm and 10-mm tumors with a 3:1 TBR.

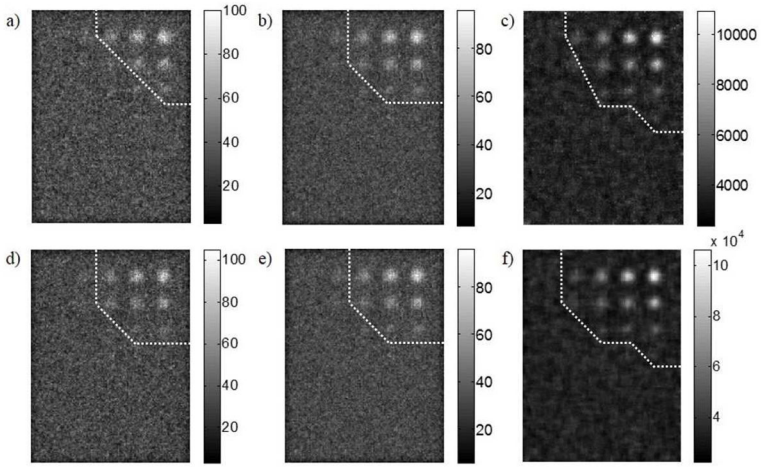

Fig. 7.

Contrast-detail projections of tumors at a 2.25-cm depth, central to the FOV. Top row: a) Inferior, b) Average, c) MIP. Bottom row: d) Superior, e) Geometric mean, f) Reprojection. Colorbar units are in counts for the planar projections and in number of emissions for the reconstructed projections. Tumors identified by the Hough transform algorithm are located above and to the right of the contrast-detail curve on each projection. The synthetic projections had the most detected low contrast hot spots, an enhancement over the individual projections.

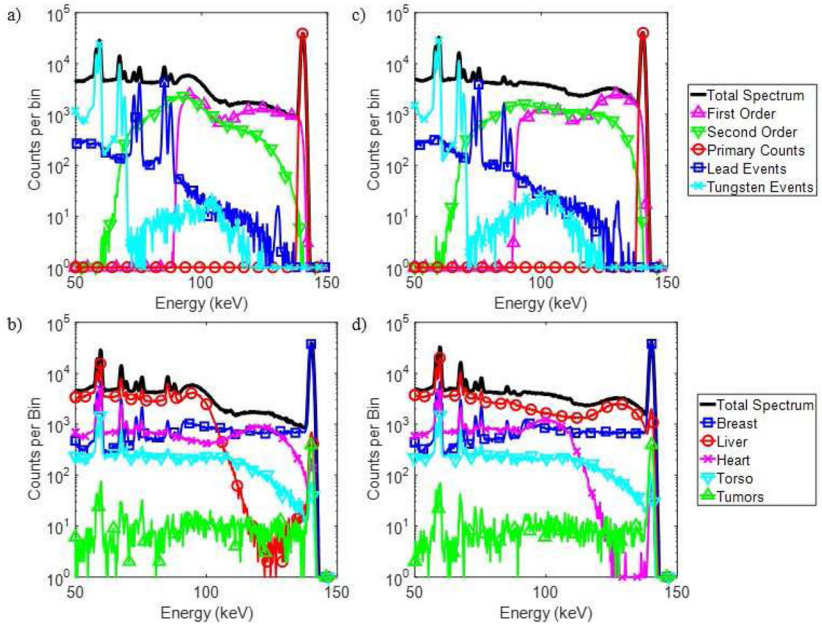

Fig. 8.

Energy spectra acquired with the inferior and superior HPGe cameras from the MBI simulations with tumors at a 2.25-cm depth. Displayed are the inferior camera's spectra parsed by a) scatter order & b) event origin and the superior camera's spectra parsed by c) scatter order & and d) event origin. The 140-keV photopeak, and subsequent projection image, contains mostly primary and first order scattered photons that originate from the breast. Gamma-rays from the organs in the torso penetrate the lead shielding of the inferior camera and follow lines of sight to the superior camera and contribute to the detector projections.

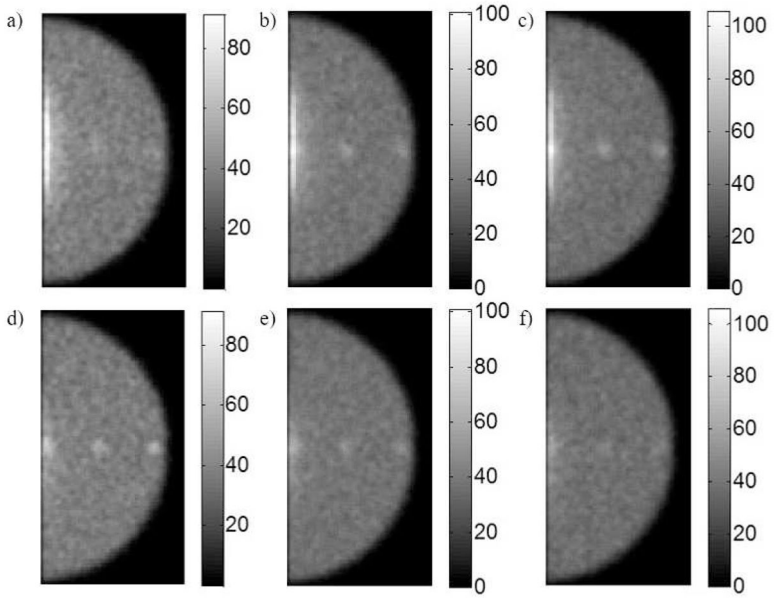

Fig. 9.

Generated planar projections of the breast phantom. Top row: Superior camera projections with tumors at a) 1-cm, b) 2.25-cm, and c) 3.5-cm depth. Bottom row: Inferior camera projections with tumors at d) 1-cm, e) 2.25-cm, and f) 3.5-cm depth. Colorbar units are in counts. The brightness of hot spots in the projections inversely correlated to detector distance from tumors. Superior projections exhibit a haze of high counts along the chest wall due to contributions from the liver.

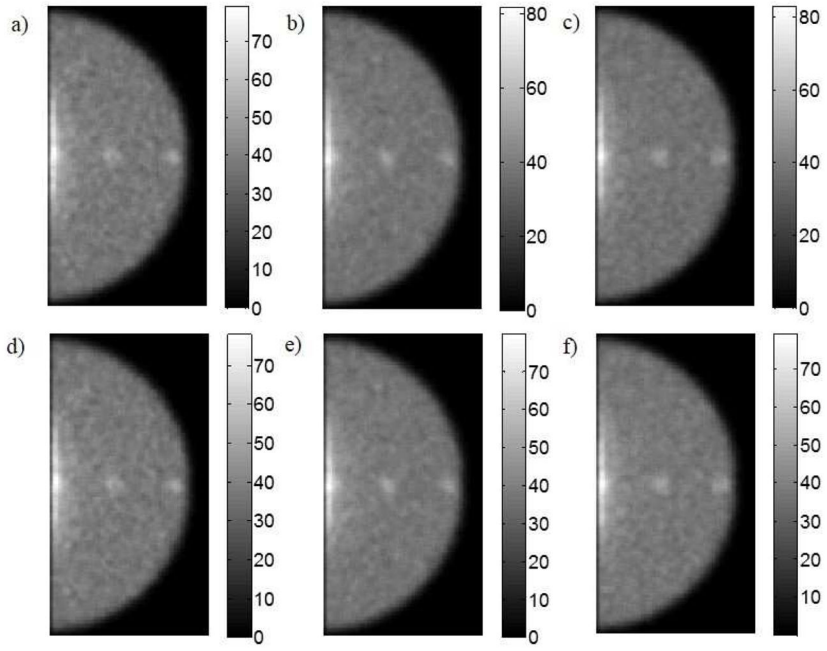

Fig. 10.

Breast projections generated using conjugate-counting methods. Top row: Average projections with tumors at a) 1-cm, b) 2.25-cm, and c) 3.5-cm depth. Bottom row: Geometric mean projections with tumors at d) 1-cm, e) 2.25-cm, and f) 3.5-cm depth. Colorbar units are in counts. All six images exhibit similar qualities. The region of high intensity counts along the chest wall found in the superior projections surrounds tumor 1. However, tumor 2 and 3 are easily observable.

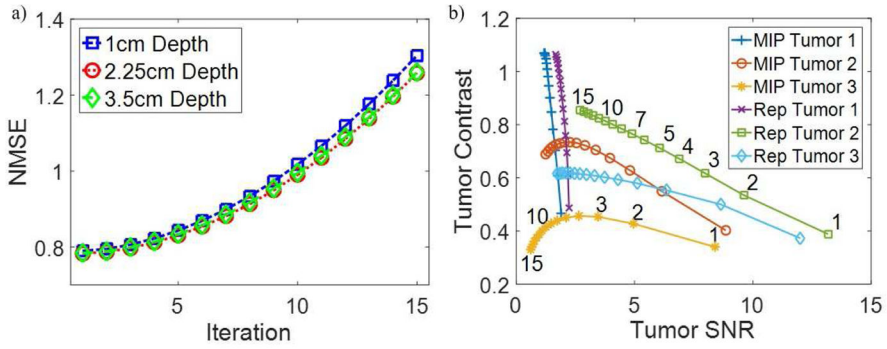

Fig. 11.

a) NMSE by iteration curves for the tomographic breast images with tumors at varying depth. All three NMSE curves monotonically increase indicating worsening reconstruction accuracy with iteration. b) A contrast versus SNR parametric plot for the 2.25 cm depth tumors in the reprojection (Rep) and MIP images. The trends of the contrast-SNR curves vary considerably for each tumor in both MIP and reprojected images. Leveraging the rising contrast and declining SNR for the various curves, and considering the parametric plot for the contrast-detail phantom (figure 4b), the third iteration is selected as the reconstructed image used to generate MIPs and reprojections for further analysis.

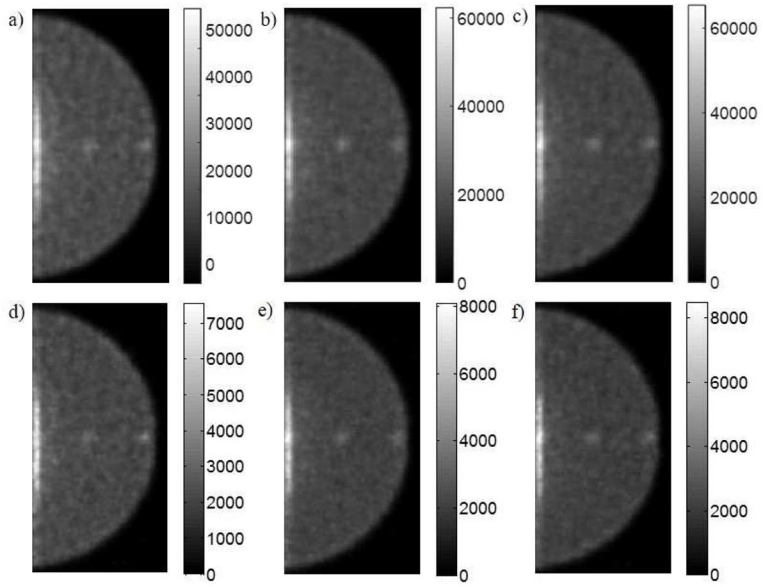

Fig. 12.

Synthetic breast phantom projections generated using the OSEM reconstruction algorithm. Top row: The reprojection of the 3D image with tumors at a) 1-cm, b) 2.25-cm, and c) 3.5-cm depth. Bottom row: The MIP of the 3D image with tumors at d) 1-cm, e) 2.25-cm, and f) 3.5-cm depth. The colorbar represents the number of emissions. Tumor 2 and 3 are observable above background in all images. The large liver signal contamination obscuring tumor 1, originally expressed in superior projections, is present in all reconstructed images.

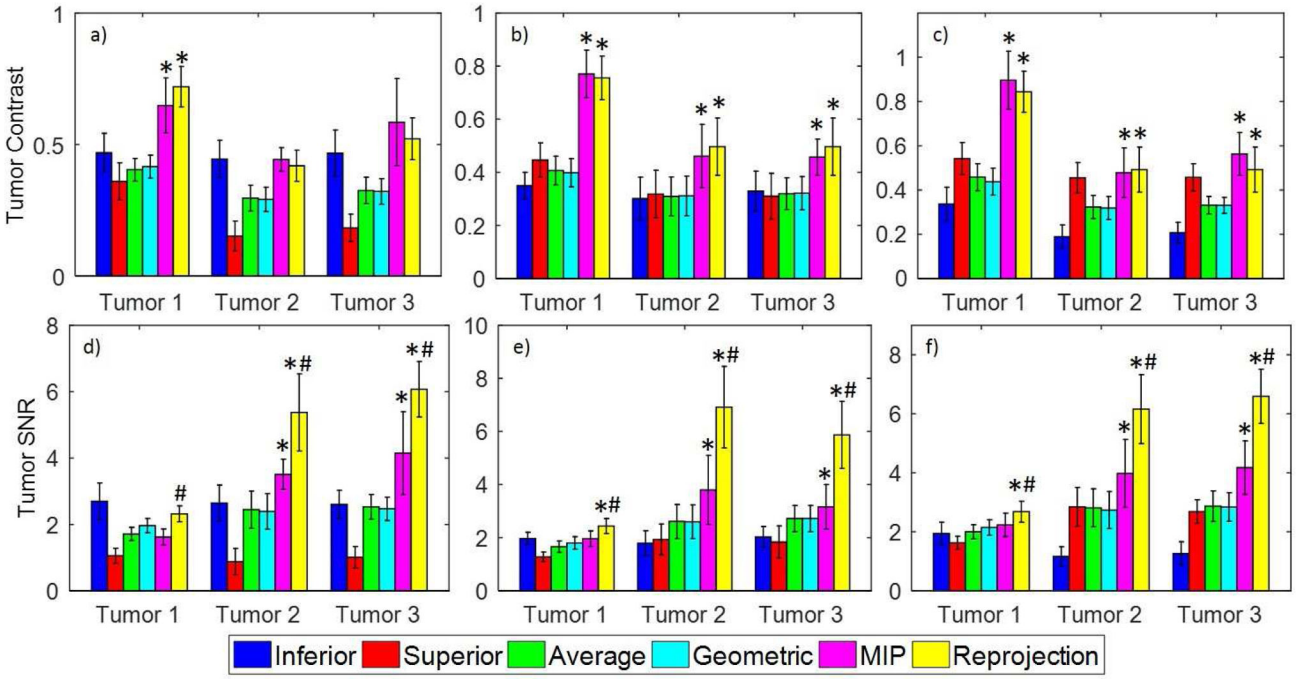

Fig. 13.

Image quality metrics of hot spots in breast projections. Top row: contrast measurements of tumors at depths of a) 1 cm, b) 2.25 cm, and c) 3.5 cm. Bottom row: SNR measurements of tumors at depths of d) 1 cm, e) 2.25 cm, f) 3.5 cm. Errorbars represent the standard deviation of measurement across the ten independent trials. The * represents a statistical difference ($p<0.05$) between the inferior projection and either the MIP or reprojection. The # represents a statistical difference ($p<0.05$) between the MIP and reprojection. Generally, the synthetic projections exhibit the highest contrast and SNR for tumors at a given depth, with the greatest SNR observed in the reprojected images.

TABLE I

Source definitions for the breast phantom with the dual-head HPGe model.

Organ	Volume (mL)	Relative Activity Conc.	Activity Conc. (MBq/mL)	Emission Probability
Liver	1200	80	0.117	0.897
Heart	250	15	0.022	0.035
Torso	6450	1	0.0014	0.060
Breast	796	1	0.0014	0.0074
Tumors	0.524	5	0.0073	2.44×10^{-5}

TABLE II

Relative count sensitivity, scatter, and torso fraction measurements.

Camera	Relative Sensitivity	Scatter Fraction	Torso Fraction
Inferior	100%	4.84%	2.98%
Superior	105.68%	7.90%	8.52%